Low loss SiN films for integrated photonics deposited by PVD at low temperature

Eva Kempf, Michele Calvo, Florian Domengie, Stephane Monfray, Frederic Boeuf, Paul Charette, Regis Orobtchouk

Research Article Vol. 13, No. 5 / 1 May 2023 / Optical Materials Express 1353
Optical Materials EXPRESS

Low loss SiN films for integrated photonics deposited by PVD at low temperature

EVA KEMPF,[1,2] MICHELE CALVO,[1] FLORIAN DOMENGIE,[1] STEPHANE MONFRAY,[1] FREDERIC BOEUF,[1] PAUL G. CHARETTE,[3] AND REGIS OROBTCHOUK[2,*]

[1] STMicroelectronics, 850 rue Jean Monnet, 38920 Crolles, France
[2] Université de Lyon, Institut des Nanotechnologies de Lyon, INSA Lyon, CNRS, UMR 5270, Lyon, France
[3] Laboratoire Nanotechnologies et Nanosystèmes (LN2), Université de Sherbrooke – 3IT, 2500 Bd de l'Université, Sherbrooke, QC J1K 2R1, Canada
[*] regis.orobtchouk@insa-lyon.fr

Abstract: Integration of SiN films with Si photonics platforms is attractive for the 3D integration of multiple waveguide levels in optical routing circuits. This paper reports on the optical characterization of SiN films deposited by PVD and PECVD with the STMicroelectronics 300 mm Photonic R&D platform at CMOS-compatible temperatures. SiN deposition was engineered to reduce the propagation losses caused by 2nd harmonic vibrational absorption of NH bonds.

1. Introduction

Silicon photonics has undergone extensive development during the last three decades thanks to the transparency and high refractive index of silicon in the near infrared, as well as advanced CMOS manufacturing, allowing size reduction and large-scale integration of passive building blocks for optical routing [1–2] and efficient modulation [3–6]. The lack of active functions such as optical sources and detectors is due to the indirect band gap of silicon. When an active device is needed, heterogeneous integration of III-V [7] and Ge on Si [8–9] materials is widely used on 300 mm wafer photonic platforms fabrication [10–11].

Nowadays, demand for integrated photonics has expanded to many fields, such as sensors, where materials other than Si are preferred, such as silicon nitride (SiN) [12]. SiN has lower thermal conductivity which is important for athermal devices and a bandgap exceeding 4 eV which avoids two-photon absorption at high power. Moreover, its lower refractive index contrast with SiO_2 reduces vertical wall roughness induced propagation losses for single mode waveguides operating just below the cutoff of the first higher order mode above the fundamental [13]. Multilayer SiN deposited by low pressure chemical vapor deposition (LPCVD) on silicon photonics substrates is available from Ligentec (thick SiN platform) [14–16], LioniX International (Triplex) [17–20], AMO GmbH (nanophotonic platform) [21–24], CNM-VLC silicon nitride platform [25–28], and IMEC (BioPIX) [29–34]. Deposition at higher temperature with LPCVD (>700°C) is preferred over plasma-enhanced chemical vapor deposition (PECVD, < 400°C) to avoid the propagation losses in the C band due to NH bonds.

Physical vapor deposition (PVD) has become attractive recently for manufacturing SiN waveguides with relatively low losses (1.6 dB/cm) at a 400°C peak processing temperature [35]. Furthermore, PVD at lower temperatures (200°C) leads to a reduction of the unwanted NH bond absorption. This paper presents two PVD low temperature SiN deposition processes for CMOS-compatible fabrication of integrated photonics devices. Basic passive integrated photonics structures were fabricated to characterize their performance compared to SiN films deposited by PECVD.

#482742 https://doi.org/10.1364/OME.482742
Journal © 2023 Received 5 Dec 2022; revised 10 Mar 2023; accepted 1 Apr 2023; published 24 Apr 2023

Optical Materials EXPRESS

2. SiN deposition process

SiN film deposition was performed on 300 mm SOI wafers (2 µm underlying thermal SiO_2 layer to prevent leakage to the substrate). SiN film thickness was fixed at 350 and 600 nm to preserve compatibility with the standard processes available on the STMicroelectronics industrial R&D platform for processing of photonic integrated circuits on 300 mm silicon-on-insulator (SOI) wafers. To overcome the losses from NH bonds resulting from PECVD deposition, we investigated PVD using RF sputtering with a silicon target and an argon/nitrogen plasma (deposition temperature below 200°C for CMOS compatibility). The stoichiometry of the plasma is varied to control the optical refractive index of the films. We compared the performance of PVD films deposited under two sets of conditions with films deposited using the standard PECVD process.

The first PVD film ("PVD 1") was deposited using a plasma of Ar and N_2 with a Ar/N_2 ratio of 0.3. The second PVD film ("PVD 2", "Si-rich") was deposited using a Ar/N_2 ratio of 0.25. Table 1 gives the thicknesses of the deposited films as well as their optical indices measured using ellipsometry and fitted with Cauchy's dispersion law.

Table 1. Thicknesses and optical refractive indexes of the SiN films deposited by PVD and PECVD

	n (λ = 1.31 µm)	n (λ = 1.55 µm)	SiN thickness
PVD 1	1.944	1.942	632 ± 8 nm
PVD 2	1.989	1.985	627 ± 16 nm
PECVD	1.913	1.910	600 ± 20 nm

3. Waveguiding component design

A variety of photonic structures such as strip waveguides, multi-mode interferometers (MMI), and ring resonators, were patterned and fabricated using the SiN films and encapsulated in TEOS silicon oxide. TE/TM mode effective indices in the strip waveguides were estimated for wavelengths between λ=1.2 µm and λ=1.7 µm using a custom-developed full vectorial finite difference mode solver [36–37]. Cartesian and cylindrical coordinates were used respectively for the design of straight and bent waveguides. Waveguides having a 600 nm thickness were designed to have a width below 700 nm, to ensure single mode operation across the considered spectral range. Transparent boundary conditions were used for the calculation of bending losses. Bending radii were set to 20 µm to limit radiative bending losses to under 0.2 dB/90° at 1.55 µm (modeled and measured bending losses are compared in the next section).

Figure 1 shows the mode solver estimations of quasi-TE mode effective index versus wavelength for 500 nm and 600 nm wide waveguides fabricated with (a) PVD1 and (b) PVD2 films. To facilitate the comparison of the mode solver predictions with experimental measurements below, 3rd order polynomial models were fitted to the mode solver results according to Eq. (1):

$$n_{eff} = a_4\lambda^3 + a_3\lambda^2 + a_2\lambda + a_1 \quad (1)$$

The mode matching method (MMM) was used to design a polarization insensitive MMI splitter. This method consists in segmenting the MMI structure into three parts (input waveguide, multimode section, output waveguides, see Fig. 2 a). A mapping of light intensity for the TE mode in the MMI splitter is shown in Fig. 2 b). For each section, both guided and radiative modes are calculated to estimate their transmission and reflection coefficients. In the input waveguide, the fundamental TE and TM modes are computed (both even), while in the output waveguide, the fundamental TE (even) and TM (odd) modes are computed. At least 5 TE and TM modes are required in the multimode section for realistic modeling of the device (scattering losses

Optical Materials EXPRESS

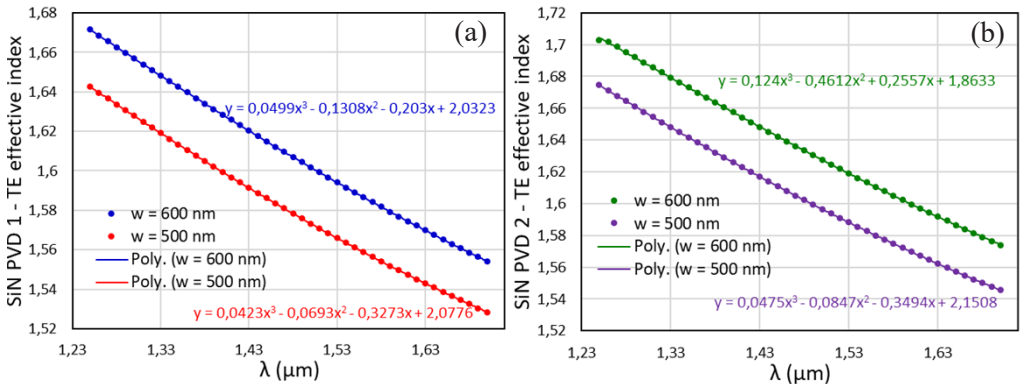

Fig. 1. Mode solver estimations (points) for quasi-TE mode effective indices for 500 nm and 600 nm wide waveguides with 3rd order polynomial fits (lines) to the mode solver data for (a) PVD 1 and (b) PVD 2 SiN films.

below 0.1 dB in the output waveguides). The smallest dimensions that satisfy this condition are a width of $W_{MMI} = 3.2$ μm and a length of $L_{MMI} = 7.7$ μm. The spacing between the output waveguides ($sp_{MMI} = 1.9$ μm) and the length of the multimode section are chosen to match the output positions of TE and TM modes in the MMI, maximizing transmission in the output waveguides. For this design, modeled transmission losses are below 0.1 dB, without the need for adiabatic tapers between the multimode section and the output waveguides.

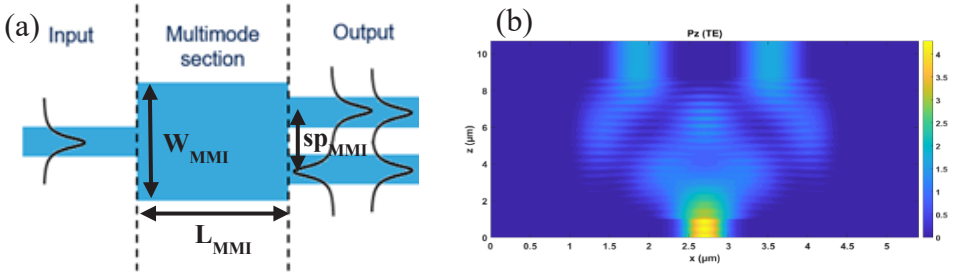

Fig. 2. (a) Geometry of the MMI and illustration of the mode matching method to model the light propagation through the splitter for the TE polarization; (b) Mapping of light intensity distribution in the MMI splitter ($W_{MMI} = 3.2$ μm, $L_{MMI} = 7.7$ μm – light propagation is from bottom to top)

4. Test structure characterization

The test structures shown in Fig. 3 were fabricated with the three SiN films of Table 1. Linear propagation losses were measured with structure (a), radiative bending losses for 20 μm radius 90° turns were measured with structure (b), and straight waveguide dispersion was measured with structure (c).

Linear propagation losses were measured using a broadband superluminescent diode (SLED) and a polarization maintaining tapered fiber to inject light by butt-coupling in the structures shown in Fig. 3(a). Transmission was measured with an optical spectrum analyzer (OSA). Loss levels were determined by differential measurements from three devices with an identical number of corner sections but with straight sections of varying length between the corners (4.2, 7 and 9.2 cm). At each wavelength, transmission measurements as a function of length were fitted

Optical Materials EXPRESS

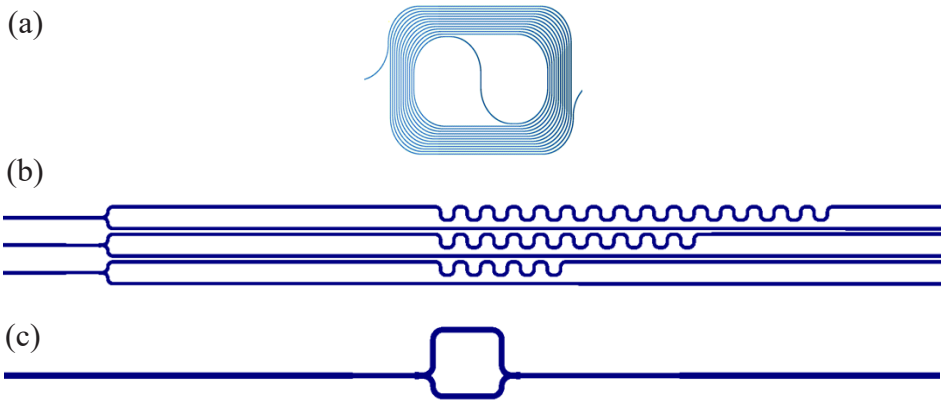

Fig. 3. Test structures used for optical characterization: (a) spirals for linear propagation loss measurements, (b) sequence of 90° turns, with 1×2 MMI splitters and straight reference arms, for bending loss measurements, (c) asymmetric Mach-Zehnder interferometer for dispersion measurements.

using linear regression where the slopes provided the propagation losses in dB/cm. The York method [38–39] was used to calculate the standard deviation between the measurements and the model using error estimations on both coordinates (0.1 μm rms error on waveguide length due to stitching effects on the UV mask, 10% rms error on output power estimated from repeated measurements).

Linear propagation losses as a function of wavelength in a 700 nm wide waveguide for the 3 film types are shown in Fig. 4 for (a) TE polarization and (b) TM polarization. The PECVD film shows low propagation losses around 1310 nm (-0.71 ± 0.11 dB/cm), whereas around 1550 nm the NH absorption peak [40] causes higher losses (-3.20 ± 0.33 dB/cm at 1560 nm). This problem was solved by the PVD 2 film which does not show any absorption peak around 1550 nm (-1.62 ± 0.11 dB/cm). However, PVD 2 shows higher losses at 1310 nm (-3.52 dB/cm ± 0.11 dB/cm). Finally, though the PVD 1 film shows an absorption peak around 1550 nm, it has lower propagation losses compared to PVD 2 at 1310 nm. While its losses are higher compared to the PECVD film at that wavelength, losses could be decreased by increasing the film density.

Quasi-TE mode bending losses though 20 μm radius 90° turns were measured using the structures shown in Fig. 3(b) having varying numbers of turns (20, 40 and 60), with a straight reference arm for normalization with respect to input power. Imbalances between the output arms of the MMI splitters were less than 0.1 dB over the measurement spectral range. Losses were calculated by first subtracting the output power from the reference arm followed by linear regression on the data, where the slope yielded the value for losses per 90° turn. As above, the York method was used to calculate the standard deviation between the measurements and the model. Figure 5 shows experimental results for 500 nm and 600 nm wide strip waveguides fabricated from PVD 1 and PVD 2 SiN films. The dashed lines show the modeled purely radiative bending losses. As seen in the figure, for wavelengths below 1450 nm, the measured losses are very close to the radiative bending losses predicted by the model. As the wavelength increases, the mode profiles widen and losses from vertical sidewall roughness become significant, adding to radiative bending losses such that the modeled and measured values diverge.

Waveguide dispersion was measured using the structures shown in Fig. 3(c). The asymmetric Mach-Zehnder interferometers (MZI) were fabricated with both 500 nm and 600 nm wide waveguides using PVD 1 and PVD 2 films. Figure 6 shows the measured and modeled values of the MZI output as a function of frequency (quasi-TE mode) for a device fabricated from 600 nm

Optical Materials EXPRESS

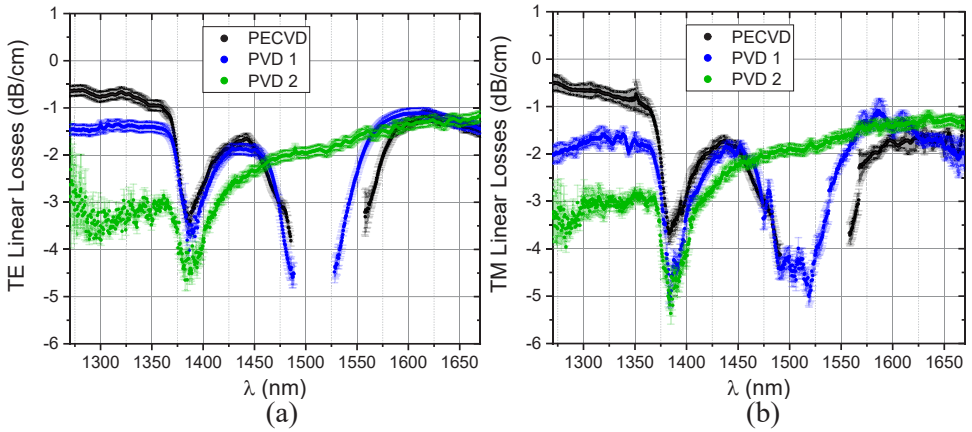

Fig. 4. Estimation of linear propagation losses from experimental measurements obtained with structures shown in Fig.3a fabricated with the three types of SiN films: (a) TE and (b) TM polarizations (700 nm width waveguides). The error bars indicate the maximum deviations from the linear regression slopes at each point (N = 3 with 4.2, 7 and 9.2 cm).

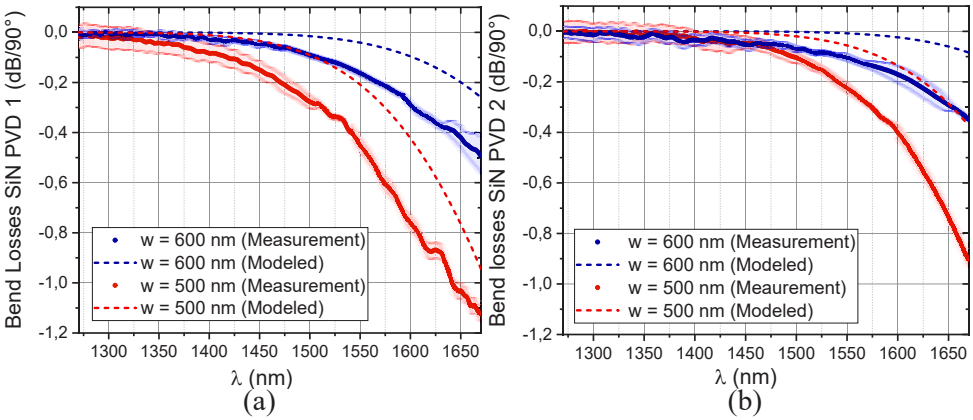

Fig. 5. Estimation of quasi-TE mode bending losses from experimental measurements through 20 µm radius 90° turns obtained with structures shown in Fig.3b for 500 nm and 600 nm width strip waveguides fabricated with (a) PVD 1 (b) PVD 2 films. The error bars indicate the maximum deviations from the linear regressions at each point (N = 4 with 0, 20, 40 and 60 bends). The dashed lines show the modeled purely radiative bending losses.

wide waveguides on PVD 1 film. The output for the MZI can be modeled as (2):

$$P_{out} = A(\lambda) \cdot \cos^2\left(\frac{\pi . n_{eff}(\lambda) \cdot \Delta L}{\lambda}\right) + \text{Offset}(\lambda) \quad (2)$$

where A(λ) is the oscillation amplitude envelope (mainly due to the power spectrum of the source), Offset(λ) is the offset from the horizontal axis due to the imbalance between the 2 arms of the MZI resulting from fabrication defects, ΔL is the length difference between the 2 arms of the MZI (100 µm by design), and n_{eff} is the mode effective index in the straight sections. The $A(\lambda)$ and Offset(λ) parameters are estimated directly from the experimental data in Fig. 6. The 5 remaining model parameters (ΔL and the a_i in n_{eff} modeled by a 3rd order polynomial) are found by Levenberg-Marquardt non-linear minimization [41] (the fitted polynomial model parameters

Optical Materials EXPRESS

in Fig. 1 and the fabrication value of ΔL are used as initial estimates). Table 2 shows fitted model parameters for 500 nm and 600 nm wide waveguides fabricated from PVD 1 and PVD 2 films.

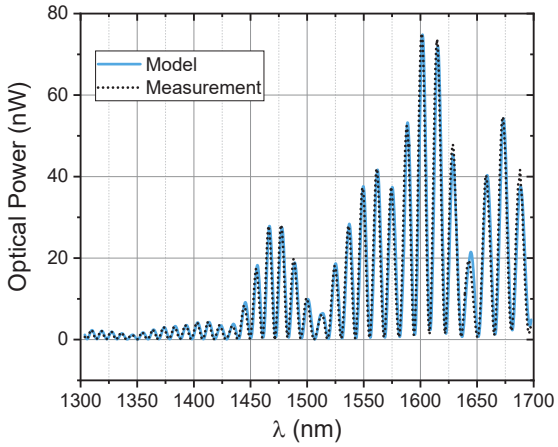

Fig. 6. Measured and modeled MZI output as a function of frequency for a device fabricated from 600 nm wide waveguides on PVD 1 film (quasi-TE mode).

Table 2. Fitted model parameters to Eq. (2) for 500 nm and 600 nm wide waveguides fabricated from PVD 1 and PVD 2 films

	a_1	a_2	a_3	a_4	ΔL (μm)
PVD 1 600 nm	2.031722	-0.207645	-0.137300	0.050496	98.54
PVD 2 600 nm	1.863484	0.262994	0.461895	0.1241670	99.42
PVD 1 500 nm	2.077583	-0.336101	-0.069309	0.040907	98.40
PVD 2 500 nm	2.150789	-0.348823	-0.085166	0.048302	99.58

Waveguide dispersion, D, is calculated as:

$$D(\mathrm{km \cdot ps^{-1} \cdot nm^{-1}}) = -\frac{\lambda}{c} \cdot \frac{\partial^2 n_{\mathrm{eff}}}{\partial \lambda^2} = -\frac{10^4}{3}(2a_3\lambda + 6a_4\lambda^2) \tag{3}$$

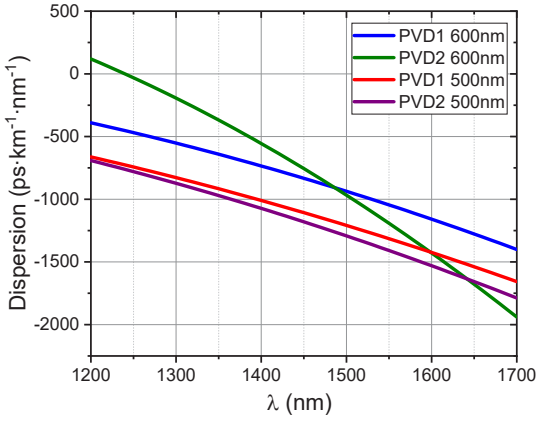

Fig. 7. Dispersion for straight waveguide sections as a function of wavelength estimated with Eq. (3) and the model parameters from Table 2. For the PVD2 film, the zero-dispersion wavelength is very close to 1310 nm.

Optical Materials EXPRESS

Figure 7 shows the resulting dispersion for straight waveguide sections as a function of frequency, estimated with Eq. (3) and the model parameters from Table 2. For the PVD 2 film, the zero-dispersion wavelength is very close to $\lambda = 1240$ nm. This characteristic can be interesting for frequency-comb generation [16].

5. Conclusion

Two types of silicon nitride films deposited by PVD with the STMicroelectronics platform were characterized in terms of linear propagations losses, bending losses, and dispersion over a 1300 nm to 1700nm bandwidth. The low temperature (200°C) deposition of PVD is compatible with the CMOS process. For the PVD 2 film, propagation losses (1.62 ±0.11 dB/cm at 1550 nm) were significantly lower compared to PECVD (>3.5 dB/cm at 1550 nm). These losses could be further reduced by increasing film density. Estimations of dispersion in the straight waveguide sections showed a near zero dispersion behavior close to 1240 nm.

Funding. European IPCEI program; IRT Nanoelec.

Disclosures. The authors declare no conflicts of interest.

Data availability. Data underlying the results presented in this paper are not publicly available at this time but may be obtained from the authors upon reasonable request.

References

1. G. Fan, R. Orobtchouk, B. Han, H. Li, C. Hu, L. Lei, H. Li, L. Xu, and Q. Wang, "Optical waveguides on three material platforms of silicon-on insulator, amorphous silicon and silicon nitride," IEEE J. Sel. Top. Quantum Electron. **22**(6), 225–231 (2016).
2. S. Guerber, C. Alonso-Ramos, D. Benedikovic, D. Pérez-Galacho, X. Le Roux, N. Vulliet, S. Crémer, L. Babaud, J. Planchot, D. Benoit, P. Chantraine, F. Leverd, D. Ristoiu, P. Grosse, D. Marris-Morini, L. Vivien, C. Baudot, and F. Boeuf, "Integrated SiN on SOI dual photonic devices for advanced Datacom solutions," Proc. SPIE **10686**, 31 (2018).
3. H. Subbaraman, X. Xu, A. Hosseini, X. Zhang, Y. Zhang, D. Kwong, and R. T. Chen, "Recent advances in silicon-based passive and active optical interconnects," Opt. Express **23**(3), 2487–2510 (2015).
4. D. Thomson, A. Zilkie, J. Bowers, T. Komljenovic, G. Reed, L. Vivien, D. Marris-Morini, E. Cassan, L. Virot, J.-M. Fedeli, J.-M. Hartmann, J. Schmid, D. Xu, F. Boeuf, P. O'Brien, G. Mashanovich, and M. Nedeljkovic, "Roadmap on silicon photonics," J. Opt. **18**(7), 073003 (2016).
5. Y. Tang, J. D. Peters, and J. E. Bowers, "Over 67 GHz bandwidth hybrid silicon electroabsorption modulator with asymmetric segmented electrode for 1.3 μm transmission," Opt. Express **20**(10), 11529–11535 (2012).
6. C. Haffner, W. Heni, Y. Fedoryshyn, J. Niegemann, A. Melikyan, D. L. Elder, B. Baeuerle, Y. Salamin, A. Josten, U. Koch, C. Hoessbacher, F. Ducry, L. Juchli, A. Emboras, D. Hillerkuss, M. Kohl, L. R. Dalton, C. Hafner, and J. Leuthold, "All-plasmonic Mach–Zehnder modulator enabling optical high-speed communication at the microscale," Nat. Phot. **9**(8), 525–528 (2015).
7. D. Liang and J. E. Bowers, "Recent progress in lasers on silicon," Nat. Photon. **4**(8), 511–517 (2010).
8. L. Vivien, A. Polzer, D. Marris-Morini, J. Osmond, J.-M. Hartmann, P. Crozat, E. Cassan, C. Kopp, H. Zimmermann, and J.-M. Fédéli, "Zero-bias 40Gbit/s germanium waveguide photodetector on silicon," Opt. Express **20**(2), 1096–1101 (2012).
9. Y. Kang, H.-D. Liu, M. Morse, M. Paniccia, M. Zadka, S. Litski, G. Sarid, A. Pauchard, Y.-H. Kuo, H.-W. Chen, W. S. Zaoui, J. Bowers, A. Beling, D. McIntosh, X. Zheng, and J. Campbell, "Monolithic germanium/silicon avalanche photodiodes with 340 GHz gain–bandwidth product," Nat. Photonics **3**(1), 59–63 (2009).
10. K. Giewont, K. Nummy, F. A. Anderson, J. Ayala, T. Barwicz, Y. Bian, K. K. Dezfulian, D. M. Gill, T. Houghton, S. Hu, B. Peng, M. Rakowski, S. Rauch, J. C. Rosenberg, A. Sahin, I. Stobert, and A. Stricker, "300-mm Monolithic Silicon Photonics Foundry Technology," IEEE J. Select. Topics Quantum Electron **25**(5), 1–11 (2019).
11. F. Boeuf, S. Crémer, and N. Vulliet, "A multi-wavelength 3D-compatible silicon photonics platform on 300 mm SOI wafers for 25Gb/s applications," in *2013 IEEE International Electron Devices Meeting*, 13.3.1-13.3.4 (2013).
12. C. Xiang, W. Jin, and J. E. Bowers, "Silicon nitride passive and active photonic integrated circuits: trends and prospects," Photonics Res. **10**(6), A82–A96 (2022).
13. D. Melati, F. Morichetti, and A. Melloni, "A unified approach for radiative losses and backscattering in optical waveguides," J. Opt. **16**(5), 055502 (2014).
14. D. T. Spencer, T. Drake, and T. C. Briles, "An optical-frequency synthesizer using integrated photonics," Nature **557**(7703), 81–85 (2018).
15. L. Chang, M. H. P. Pfeiffer, N. Volet, M. Zervas, J. D. Peters, C. L. Manganelli, E. J. Stanton, Y. Li, T. J. Kippenberg, and J. E. Bowers, "Heterogeneous integration of lithium niobate and silicon nitride waveguides for wafer-scale photonic integrated circuits on silicon," Opt. Lett. **42**(4), 803–806 (2017).

Optical Materials EXPRESS

16. V. Brasch, M. Geiselmann, T. Herr, G. Lihachev, M. H. P. Pfeiffer, M. L. Gorodetsky, and T. J. Kippenberg, "Photonic chip based optical frequency comb using soliton Cherenkow radiation," Science **351**(6271), 357–360 (2016).
17. D. J. Blumenthal, R. Heideman, D. Geuzebroek, A. Leinse, and C. Roeloffzen, "Silicon nitride in silicon photonics," Proc. IEEE **106**(12), 2209–2231 (2018).
18. C. G. H. Roeloffzen, M. Hoekman, and E. J. Klein, "Low-loss Si3N4 TriPleX optical waveguides: technology and applications overview," IEEE J. Select. Topics Quantum Electron. **24**(4), 1–21 (2018).
19. K. Worhof, R. G. Heideman, A. Leinse, and M. Hoekman, "TriPleX: a versatile dielectric photonic platform, advanced optical technologies," Adv. Opt. Technol. **4**(2), 189–207 (2015).
20. PiX4life, Pilot line. [Online]. Available: www.pix4life.eu
21. M. A. Piqueras, T. Mengual, B. Chmielak, A. Catalani, P. Huggard, H. Wang, and R. Ortuño, "Photonic front-end for the next-generation of space SAR applications," Proc. SPIE **9639**, 96391I (2015).
22. G. Dabos, D. Ketzaki, A. Manolis, L. Markey, J. C. Weeber, A. Dereux, A. L. Giesecke, C. Porschatis, B. Chmielak, D. Tsiokos, and N. Pleros, "Plasmonic Stripes in Aqueous Environment Co-Integrated with Si3N4 Photonics," IEEE Photonics J. **10**(1), 1–8 (2018).
23. P. J. Cegielski, A. L. Giesecke, S. Neutzner, C. Porschatis, M. Gandini, D. Schall, C. A. R. Perini, J. Bolten, S. Suckow, S. Kataria, B. Chmielak, T. Wahlbrink, A. Petrozza, and M. C. Lemme, "Monolithically integrated perovskite semiconductor lasers on silicon photonic chips by scalable top-down fabrication," Nano Lett. **18**(11), 6915–6923 (2018).
24. P. J. Cegielski, S. Neutzner, C. Porschatis, H. Lerch, J. Bolten, S. Suckow, A. R. S. Kandada, B. Chmielak, A. Petrozza, T. Wahlbrink, and A. L. Giesecke, "Integrated perovskite lasers on a silicon nitride waveguide platform by cost-effective high throughput fabrication," Opt. Express **25**(12), 13199–13206 (2017).
25. L. A. Bru, D. Pastor, and P. Munoz, "Integrated optical frequency domain reflectometry device for characterization of complex integrated devices," Opt. Express **26**(23), 30000–30008 (2018).
26. D. Pérez, I. Gasulla, and J. Capmany, "Field-programmable photonic arrays," Opt. Express **26**(21), 27265–27278 (2018).
27. K. E. Zinoviev, A. B. González-Guerrero, C. Domínguez, and L. M. Lechuga, "Integrated bimodal waveguide interferometric biosensor for label-free analysis," J. Lightwave Technol. **29**(13), 1926–1930 (2011).
28. J.-C. Tinguely, Ø. I. Helle, and B. S. Ahluwalia, "Silicon nitride waveguide platform for fluorescence microscopy of living cells," Opt. Express **25**(22), 27678–27690 (2017).
29. M. U. Hasan, P. Neutens, R. Vos, L. Lagae, and P. Van Dorpe, "Suppression of bulk fluorescence noise by combining waveguide-based near-field excitation and collection," ACS Photonics **4**(3), 495–500 (2017).
30. S. Kerman, D. Vercruysse, T. Claes, A. Stassen, M. U. Hasan, P. Neutens, V. Mukund, N. Verellen, X. Rottenberg, L. Lagae, and P. Van Dorpe, "Integrated nanophotonic excitation and detection of fluorescent microparticles," ACS Photonics **4**(8), 1937–1944 (2017).
31. A. Dhakal, A. Z. Subramanian, P. Wuytens, F. Peyskens, N. Le Thomas, and R. l Baets, "Evanescent excitation and collection of spontaneous Raman spectra using silicon nitride nanophotonic waveguides," Opt. Lett. **39**(13), 4025–4028 (2014).
32. A. Z. Subramanian, P. Neutens, A. Dhakal, R. Jansen, T. Claes, X. Rottenberg, F. Peyskens, S. Selvaraja, P. Helin, B. Du Bois, K. Leyssens, S. Severi, P. Deshpande, R. Baets, and P. Van Dorpe, "Low-loss singlemode PECVD silicon nitride photonic wire waveguides for 532–900 nm wavelength window fabricated within a CMOS pilot line," IEEE Photonics J. **5**(6), 2202809 (2013).
33. H. Jans, P. O'Brien, I. Artundo, M. A. G. Porcel, R. Hoofman, D. Geuzebroek, P. Dumon, M. Van der Vliet, J. Witzens, E. Bourguignon, P. Van Dorpe, and L. Lagae, "Integrated bio-photonics to revolutionize health care enabled through PIX4life and PIXAPP," Proc. SPIE **10506**, 31 (2018).
34. D. Martens, A. Z. Subramanian, S. Pathak, M. Vanslembrouck, P. Bienstman, W. Bogaerts, and R. G. Baets, "Compact silicon nitride arrayed waveguide gratings for very near-infrared wavelengths," IEEE Photon. Technol. Lett. **27**(2), 137–140 (2015).
35. A. Frigg, A. Boes, G. Ren, T. G. Nguyen, D.-Y. Choi, S. Gees, D. Moss, and A. Mitchell, "Optical frequency comb generation with low temperature reactive sputtered silicon nitride waveguides," APL Photonics **5**(1), 011302 (2020).
36. X. Hu, S. Cueff, P. Rojo Romeo, and R. Orobtchouk, "Modeling the anisotropic electro-optic interaction in hybrid silicon-ferroelectric optical modulator," Opt. Express **23**(2), 1699–1714 (2015).
37. M. Masi, R. Orobtchouk, G. F. Fan, and L. Pavesi, "Towards a realistic modeling of ultra-compact racetrack resonators," Journ. of Light. Techn. **28**(22), 3233–3242 (2010).
38. D. York, "Least-squares fitting of a straight line," Can. J. Phys. **44**(5), 1079–1086 (1966).
39. D. York, N. M. Evensen, M. López Martínez, and J. De Basabe Delgad, "Unified equations for the slope, intercept, and standard errors of the best straight line," Am. J. Phys. **72**(3), 367–375 (2004).
40. C. H. Henry, R. F. Kazarinov, H. J. Lee, K. J. Orlowsky, and L. E. Katz, "Low loss Si_3N_4–SiO_2 optical waveguides on Si," Appl. Opt. **26**(13), 2621–2624 (1987).
41. W. H. Press, S. A. Teukolsky, H. A. Bethe, W. T. Vetterling, and P. Flannery, *Numerical Recipes: The Art of Numerical Computing*, (Cambridge University Press, 2007).